UDK 691.714:52-17:666.9.04
Original scientific article/Izvirni znanstveni članek

ISSN 1580-2949
Mater. Tehnol.

NUMERICAL SIMULATION AND EXPERIMENTAL VERIFICATION OF HEAT TREATMENT OF A SADDLE HOLLOW TUBE

NUMERIČNA SIMULACIJA IN EKSPERIMENTALNA VERIFIKACIJA PROCESA TOPLOTNE OBDELAVE VOTLE CEVI ZA SEDEŽE KOLES

Weichi Pei[1], Jiawang Zhang[1], Rongdi Yu[2], Qing Huang[3], Shengqiang Liu[1], Menglong Xing[1], Hongchao Ji[1]*

[1]College of Mechanical Engineering, North China University of Science and Technology, Tangshan 063210, China
[2]Tangshan Chenyang Sports Equipment Co., Ltd., Hebei, Tangshan 063399, China
[3]Beijing Satellite Manufacturing Factory Co., Ltd., Beijing, Haidian 100094, China

Prejem rokopisa – received: 2025-06-06; sprejem za objavo – accepted for publication: 2025-10-07

doi:10.17222/mit.2025.1473

To study the microstructure evolution of 42CrMo steel saddle-shaped hollow tubes during heat treatment, this study integrates numerical simulation with experimental validation, establishing a thermophysical database developed in JMatPro software and coupled with a DEFORM-based 3D finite element model for multiphysics-coupled quenching-tempering simulations. Four monitoring nodes (P1–P4) recorded temperature field variations and microstructure evolution. The results show that the simulated microstructure evolution agrees with the predictive law of continuous cooling phase transition. After quenching, a metallographic structure mainly composed of martensite is formed, and it transforms into tempered sorbite during tempering. Eventually, a typical tempered sorbite-ferrite dual-phase structure is formed, and there is no obvious tendency of tempering brittleness. The actual experiment is basically consistent with the simulation results. The geometric parameters (wall thickness, radius of curvature) had a relatively small influence on the uniformity of microstructure transformation, confirming the effectiveness of the heat-treatment parameters.

Keywords: 42CrMo steel, numerical simulation, microstructure, phase transformation mechanism

Avtorji v članku opisujejo študijo zakonov razvoja mikrostrukture toplotno obdelanega jekla tipa 42CrMo iz katerega so izdelane votle cevi za sedeže koles, ki imajo specifičo obliko. V tej študiji so avtorji vključili poleg eksperimentalnega ovrednotenja še numerično simulacijo. Za to so uporabili razpoložljive termofizikalne podatke iz programske opreme JmatPro v povezavi s 3D modelom, ki temelji na programski opremi DEFORM oziroma profesionalni metodi končnih eklementov za večfizikalno povezane simulacije procesov poboljšanja jekel; to je: kaljenja in popuščanja. Izbrali so štiri nadzorna vozlišča (P1–P4), ki so beležila spremembe temperaturnega polja in razvoj mikrostrukture. Rezultati simulacij so pokazali, da proces razvoja mikrostrukture ustreza napovednemu zakonu faznega prehoda med neprekinjenim ohlajanjem. Po kaljenju je imelo jeklo v glavnem martenzitno mikrostrukturo, ki pa se je po popuščanju spremenila (transformirala) v popuščni sorbit. V nekaterih primerih lahko pride tudi do nastanka tipične popuščne sorbitno-feritne mikrostrukture, ki pa ne kaže očitne nagnjenosti k popuščni krhkosti. Dejanski preizkusi so se v osnovi ujemali z rezultati simulacije. Geometrijski parametri (debelina stene, polmer ukrivljenosti) imajo relativno majhen vpliv na enovitost nastale mikrostrukture, kar potrjuje učinkovitost izbranih procesnih parametrov toplotne obdelave.

Ključne besede: jeklo tipa 42CrMo, numerična simulacija, mikrostruktura, mehanizem fazne transformacije

1 INTRODUCTION

Functioning as a critical load-bearing component between the saddle structure and seatpost in bicycle frames, the saddle hollow tube must sustain multiaxial loading during service, necessitating materials with superior comprehensive mechanical properties. The 42CrMo low-alloy steel has been extensively employed for this application due to its optimal balance of hardenability, low-temperature toughness, fatigue-impact resistance, and formability, alongside minimized temper brittleness susceptibility.[1–4] Following cold-drawn forming, components undergo controlled heat treatments to achieve targeted microstructures and mechanical properties, with precise parameter regulation governing the martensite/bainite phase ratio and grain refinement. Appropriate heat treatment temperature and holding time can enhance the mechanical properties of steel, and the metallographic structure produced at a certain temperature and holding time can enable steel to achieve better hardness and wear resistance.[5]

Recent investigations have focused on optimizing the heat treatment of 42CrMo steel, with quenching and tempering emerging as standard protocols supported by extensive research.[6,7] After careful analysis of the heat treatment process involving conventional heat treatment and subsequent quenching-and-tempering treatments,

*Corresponding author's e-mail:
jihongchao@ncst.edu.cn (Hongchao Ji)

Bilal et al.[8] conducted a study on the changes in the organizational structure and mechanical properties of 42CrMo steel. Comparing the traditional heat-treated specimens with those subjected to secondary quenching and tempering, the researchers observed that the mechanical properties of the latter were superior to those of the primary quenched-and-tempered specimens. The most significant improvement was noted in terms of toughness, which can be attributed to the finer martensitic organization achieved through the subsequent quenching-and-tempering process compared to the traditional heat-treatment method.

Ji et al.[9] reported that the martensite content decreases with both increasing quenching temperature and extending quenching holding time during isothermal quenching. Lv et al.[10] conducted a comparative analysis of the properties of warm rolled steel and conventionally quenched and tempered steel, revealing that the yield ratio of tempered steel after quenching at 150 °C significantly exceeds that of warm rolled steel. Qin et al.,[11] after their investigation involving 42CrMo bearing ring tempering experiments, reported that when the quenching temperature remains constant, higher tempering temperatures facilitate the transformation and dissolution of quenched martensite, resulting in the precipitation of a small number of uniformly distributed tiny carbide particles. The carbide content is proportional to the toughness of steel. Sanij et al.[12] compared the effects of conventional and double tempering techniques used on AISI 4140 steel and reported that both processes resulted in comparable hardness and strength levels. However, the double tempered steel exhibited a 23 % improvement in impact toughness and led to a finer austenite grain structure.

As a result of the superior hardenability of 42CrMo steel, it is prone to the formation of quenching cracks during heat treatment due to its rapid temperature gradient during cooling from high to low temperatures. This process leads to the initiation and propagation of microcracks in the martensitic structure as a result of localized stresses generated by excessive cooling rates and manifested as quenching cracks in the material.[13,14] Wang et al.[15] conducted a fracture failure analysis of 42CrMo steel crankshafts from heavy trucks, revealing that while the metallurgical transformation induced by high temperatures contributes to certain properties, it also exerts some influence on the susceptibility to fracture failure in specific cases.

Silva et al.[16] conducted numerical simulations of a quenching process involving AISI 4140 steel C-ring specimens, utilizing DEFORM and JMatPro software to perform finite element modeling. The simulation results demonstrated a strong correlation with the experimental data, validating the accuracy of the finite element model. Qian et al.[17] performed a comprehensive analysis of 42CrMo steel ring-shaped workpieces during quenching by combining macroscopic and microscopic three-dimensional finite element simulations using ABAQUS software. They analyzed the quenching process from unloading to afterheat conditions, providing detailed insights into the behavior of the material under different cooling scenarios. Gao et al.[18] investigated microstructure transformation during quenching of 42CrMo steel vehicle front axles through finite element simulation and conducted experimental verification to ensure the accuracy of the simulation results. This multi-methods approach provided a robust foundation for understanding the mechanics of quenching processes in complex engineering applications.

This paper investigates the quenching and tempering processes of hollow-tube 42CrMo steel saddles through a combination of finite element simulation, X-ray diffraction experiments, metallographic experiments, and numerical simulations using JMatPro and DEFORM software. The study systematically analyzed the metallurgical structure transformation mechanisms and compared the results of finite element simulations with experimental data to validate the simulation models. Further improvements were achieved by integrating these methods, providing a comprehensive understanding of the material's behavior during heat treatment and structural transformation processes.

2 NUMERICAL MODELING AND EXPERIMENTAL DETAILS

2.1 Experimental details

The chemical composition of 42CrMo steel used in this study is shown in **Table 1**. It was examined with an X-ray fluorescence spectrometer (ZSX Primus II).

Table 1: Chemical composition of 42CrMo steel (*w*/%)

Element	C	Si	Mn	Cr	S	P	Mo	Fe
Mass fraction *w*/%	0.41	0.28	0.74	1.048	0.006	0.011	0.182	Bal.

The maximum hardness of quenched steel is influenced by the carbon content, and carbon is also the most effective element for delaying bainite transformation and stabilizing austenite.[19] Other alloying elements also exert specific effects on hardenability. Chromium (Cr) inhibits the diffusion of carbon atoms in steel. Notably, it prevents the formation of bainite and pearlite while promoting martensitic transformation. Additionally, Cr facilitates the transformation of martensite at lower quenching rates, thereby enhancing steel's hardenability. Similarly, manganese (Mn) and molybdenum (Mo) segregate preferentially at grain boundaries, which in turn hinder the transformation of ferrite to pearlite.[20–22]

The structure of the saddle hollow tube is shown schematically in **Figure 1**. **Figure 1a** illustrates the position of the hollow tube of the saddle on the bicycle; **Figure 1b** is a schematic diagram of the physical object. In order to study the influence of the geometry of the saddle

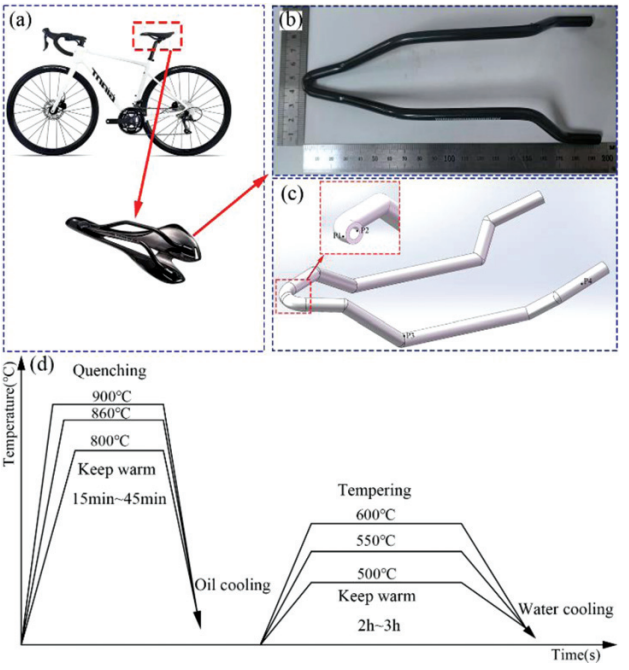

Figure 1: Saddle hollow tube schematic

hollow tube on the microstructure evolution, four characteristic nodes were selected on the hollow tube. **Figure 1c** is a schematic diagram of the four selected feature nodes. P1 denotes the outer wall of the hollow tube at the bend, and P2 denotes on the inner wall of the same bend with a hollow-tube wall thickness of approximately 1.75 mm. P3 represents the region at the bend of the tube, while P4 corresponds to the straight outer surface of the hollow tube.

Figure 1d illustrates the heat-treatment flow of the saddle hollow tube. Quenching is carried out at (800, 860 and 900) °C and held for 15 min to 45 min, followed by oil cooling. Then, tempering is conducted in high-temperature box-type resistance furnaces at (500, 550 and 600) °C for 2 h to 3 h, and finally water cooling is performed. All the samples were heated up along with the furnace.

The hollow tubes were cut using a wire cutting machine, and the metallographic structures of the four characteristic nodes after treatment were analyzed in detail by an optical microscope (OM) and an X-ray diffractometer (XRD). Subsequently, tensile tests were conducted on the tempered specimens, with the aim of revealing, from different perspectives, the evolution laws and mechanical property changes in different phase structures of 42CrMo steel during heat treatment, thereby clarifying the mechanism of microstructure phase transformation of 42CrMo steel.

2.2 Simulation of thermodynamic parameters of the material

After obtaining the specific chemical composition of 42CrMo steel, the thermodynamic performance parameters, CCT curve and TTT curve of 42CrMo steel were simulated using JMatPro. **Figure 2a** shows the thermal conductivity and specific heat capacity of 42CrMo steel; **Figure 2b** shows the resistivity and electrical conductivity of 42CrMo steel; **Figure 2c** shows the hardenability curve of 42CrMo steel; **Figure 2d** shows the phase properties of 42CrMo steel; **Figure 2e** shows the CCT curve of 42CrMo steel; **Figure 2f** shows the TTT curve of 42CrMo steel.

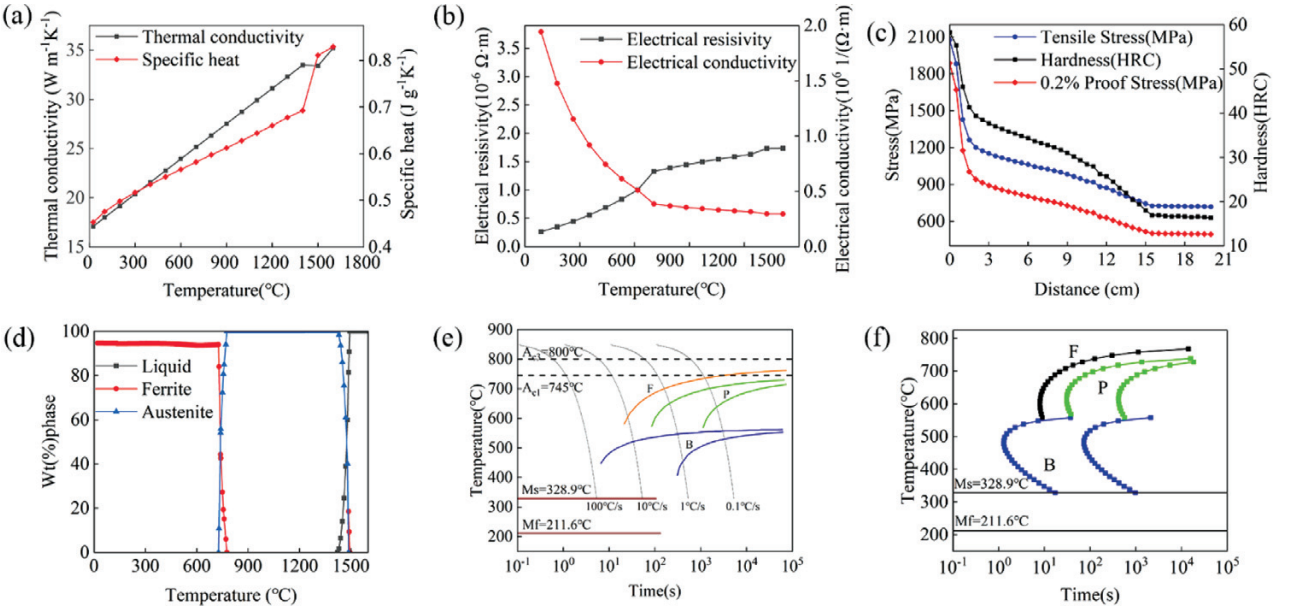

Figure 2: Thermodynamic performance parameter diagram of 42CrMo steel

3 NUMERICAL SIMULATION RESULTS AND EXPERIMENTAL VALIDATION

3.1 Quenching simulation and experimentation

Before the numerical simulation analysis, pre-processing was performed. Using SolidWorks for 3D finite element modeling, the 3D model and the thermodynamic material parameters of 42CrMo steel, previously simulated with JmatPro, were imported into DEFORM. The grid was tetrahedral, with a set quantity of 100,000. The initial temperature was 20 °C, the heating rate was 10 °C/min, the heating diffusion coefficient was 0.1 N/s/mm/C, the thermal conductivity coefficient of the oil was 5.5 N/s/mm/C, and the heat exchange coefficient with air was 0.2 N/s/mm/C. The microstructure cloud diagram of the quenching stage is shown in **Figure 3**.

When the quenching temperature is 800 °C, incomplete austenitization leads to low austenite volume fraction, insufficient diffusion of carbon, and high residual ferrite content (**Figure 3a2**), hindering the efficiency of martensitic transformation. After quenching, the maximum martensitic volume fraction is only 0.661.

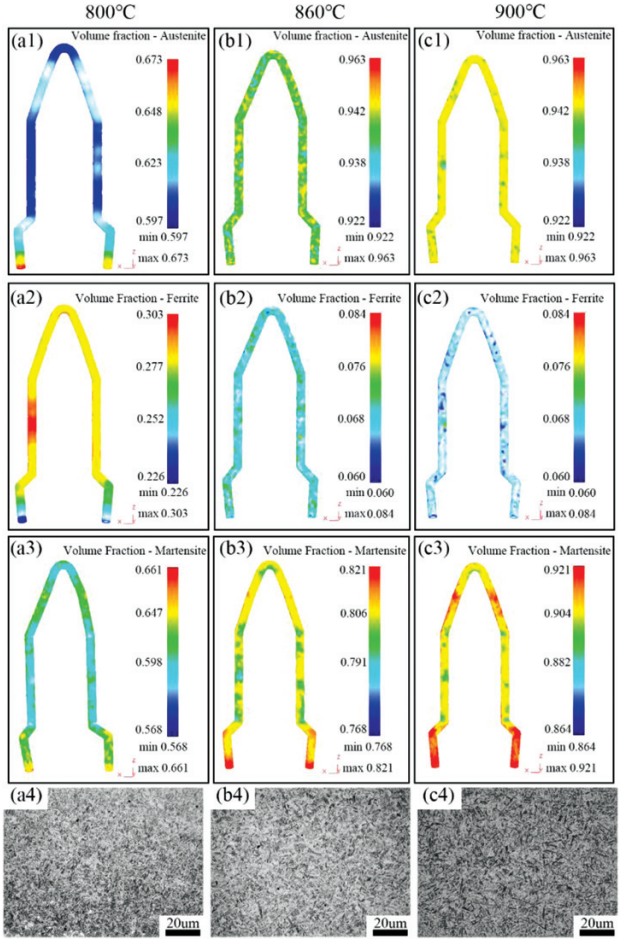

Figure 3: Microstructure cloud diagrams and metallographic structures at different quenching temperatures

At an elevated temperature of 860 °C, the austenite volume fraction increased significantly and the ferrite residue plummeted to 0.060–0.084 (**Figure 3b2**). After quenching and cooling, the martensitic volume fraction was elevated to 0.768–0.821. The homogenization of austenite and full dissolution of carbon provided the basis for an efficient martensitic transformation, while the organization homogeneity and the efficiency of the phase transition reached the optimum. After further heating up to 900 °C, the austenite volume fraction remained high and the martensitic volume fraction further increased to 0.864–0.921. However, high temperature may trigger the coarsening of the austenite grains, with the risk of weakening the grain boundaries.

Figures 3a4–c4 show the metallographic structures of 42CrMo steel corresponding to different quenching temperatures. At the quenching temperature of 800 °C, the complete austenitization temperature was not reached, leading to partial austenitization, as shown in **Figure 3a4**. As a result, the microstructure consisted of undissolved massive ferrite and carbides coexisting with quenched fine lath martensite. The grain boundaries were prone to stress concentration, causing a decline in both material hardness and toughness.

When quenched at 860 °C, as shown in **Figure 3b4**, austenitization was fully completed. Carbon and alloying elements were uniformly solidified in the matrix. Oil cooling produced a fine, uniform and dense lath martensitic structure with a low content of retained austenite. The grain boundaries were distinct, and the grain size was fine, enabling the material to achieve excellent comprehensive mechanical properties.

With further increase in the quenching temperature to 900 °C (**Figure 3c4**), the austenite grains were coarsened significantly due to overheating, leading to the formation of coarse lath martensite after quenching. Meanwhile, the solid solution of carbon and alloying elements inhibited the transformation from austenite to martensite, resulting in a decrease in the M_s point and an increase in the proportion of retained austenite. Additionally, the weakened grain boundaries and inhomogeneous microstructure intensified the degradation of impact toughness and fatigue strength, leading to a significant reduction in both properties.

Figures 4a and **4b** show the changing trends of austenite and pearlite at four characteristic nodes of the saddle hollow tube during the quenching and heating stage. **Figures 4c–4f** show the changing trends of the microstructures of the four characteristic nodes of the saddle hollow tube during oil cooling. The start time of oil cooling is 5400 s. The period before 5400 s is the quenching heating stage, and the period after that is the oil cooling stage.

Figures 4 P1–P4 show metallographic structure diagrams of the four characteristic nodes of the saddle hollow tube after quenching at 860 °C. It can be concluded from the curve graphs that during quenching, the

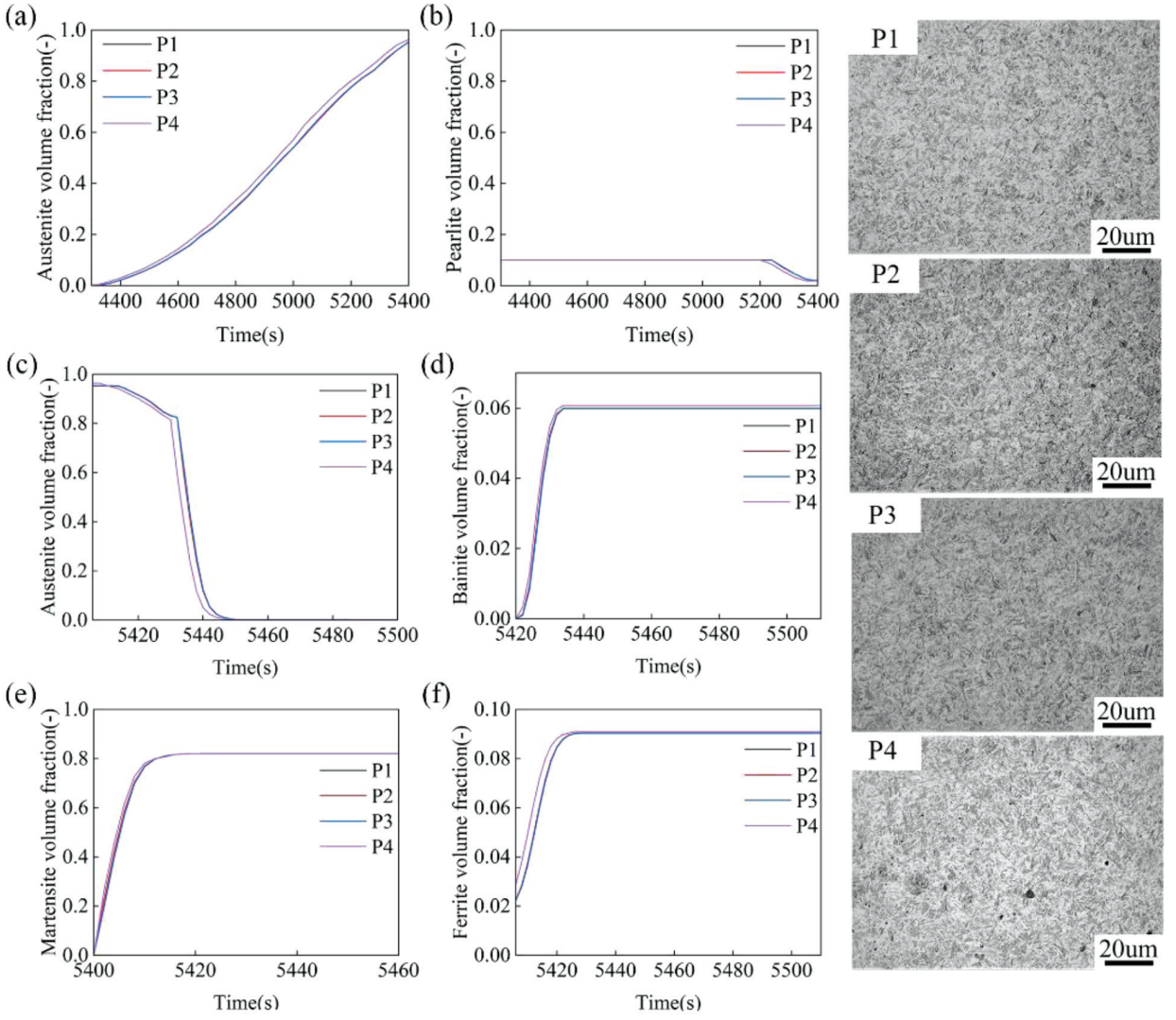

Figure 4: Microstructural variation and metallographic organization of characteristic nodes during quenching

microstructural evolution dynamics of the four characteristic nodes show similar change patterns. Among these nodes, P1 (outer wall node) and P2 (inner wall node) are constrained by geometric factors, such as a wall thickness of approximately 1.75 mm. However, they exhibit a phase transformation behavior comparable to the other nodes as the impact of the wall thickness on the martensite and austenite phase transformations is relatively low.

It is worth noting that the P3 node, located in the bending region, displays a highly consistent phase-transformation kinetic curve, similar to those of P1 and P2, despite exhibiting stress concentration effects. In contrast, the P4 node, positioned within the straight tube section, displays a unique phase transformation behavior: during the initial heating stage, its austenite phase transformation rate is significantly higher than that of the other nodes, by approximately 23 %, which can primarily be attributed to favorable heat-transfer boundary conditions in this region. At the end of the quenching stage, the final volume fraction of austenite at the P4 node is close to 96 %, which is 0.011 higher than that of the node with the lowest austenite volume fraction.

This diffusive phase transformation mechanism directly leads to the failure of the specimen cross-section, obtaining martensite-dominated microstructural characteristics, with an average bainite volume fraction of 6 % and an average ferrite percentage of 6 % in the phase composition. This phenomenon is consistent with the theoretical predictions of the CCT curve for the cooling kinetics of medium-carbon alloy steels.

The analysis of the characteristic nodal-microstructure content change curves reveals that a rapid transformation of austenite into martensite can be observed within a very short time after the start of oil cooling. This phenomenon is mainly determined by the cooling rate, which leads to further transformation of a small amount of austenite to ferrite and bainite. Combined with the metallographic analysis of each stage of the microstructure by optical microscopy, it can be observed,

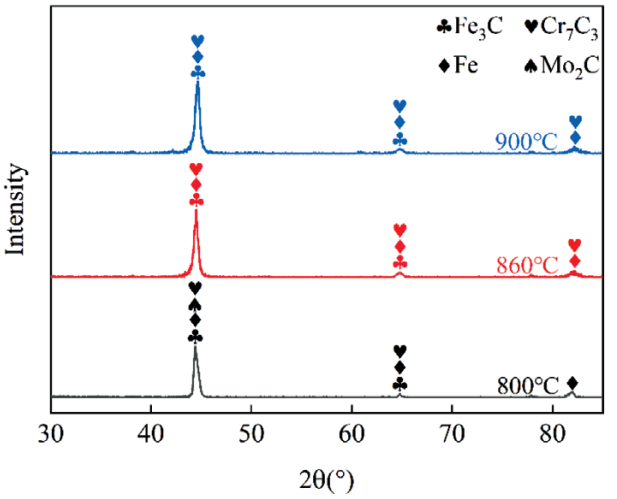

Figure 5: XRD pattern of 42CrMo steel at different quenching temperatures

in **Figure 4** P1–P4, that the lath-like structure occupies about 80 %, indicating that it is a martensitic organization.[23,24] Bainite is distributed in the form of clusters or strips, while carbides are present in the form of fine particles in the substrate, further verifying the complex multiphase transformation mechanism of the specimen during oil cooling.

By combining the metallographic structure of 42CrMo steel at different quenching temperatures (**Figure 3**) with the XRD patterns (**Figure 5**), it can be found that when quenched at 800 °C, the iron peak intensity is moderate, indicating the presence of undissolved ferrite or low-carbon martensite. The persistent residual Fe_3C peak reflects the incomplete austenitization process, leading to the carburized body not being dissolved completely. Additionally, the absence of Cr_7C_3/Mo_2C peaks suggests that the Cr/Mo diffusion is insufficient to inhibit the formation of alloy carbides, resulting in a microstructure characterized by coexisting undissolved ferrite and coarse carbides, along with a small and uneven martensite formation.

When the temperature increases to 860 °C, the intensity of the Fe peaks becomes the sharpest, corresponding to the complete austenitization of high-carbon martensite. The disappearance of the Fe_3C peak indicates that all carbides were dissolved, while the enhancement of Cr_7C_3/Mo_2C peaks shows that the Cr/Mo diffusion is sufficient, forming a stable carbonite. This process is accompanied by significant incomplete austenitization, which prevents a complete dissolution of certain carbides, while the Cr/Mo diffusion continues to optimize the microstructure. The resulting metallographic organization exhibits a uniform distribution of fine slate

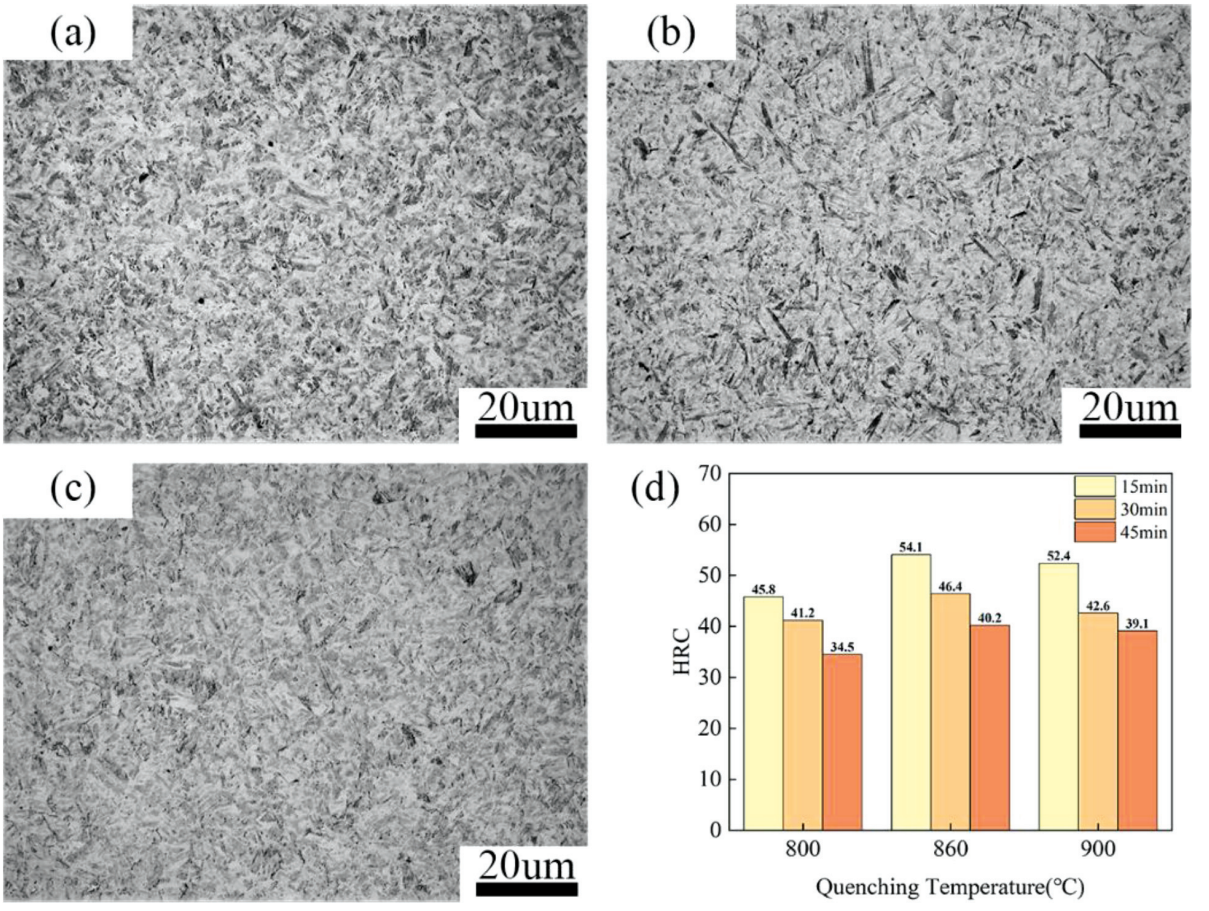

Figure 6: Metallographic structure of 42CrMo steel and the Rockwell hardness of the quenched samples under different quenching holding times

martensite and dispered carbides, effectively inhibiting grain boundary migration.

Upon further increase in the quenching temperature to 900 °C, the intensity of the Fe peaks slightly decreases, suggesting a certain degree of carbon dissolution and alloying element diffusion. However, this temperature also leads to the reappearance of Fe_3C peaks, along with a significant strengthening of the Cr_7C_3 peaks. This indicates that while the degree of austenitization initially increases, beyond a certain threshold, it destabilizes the dissolution-precipitation equilibrium, resulting in incomplete dissolution of some carbides. Concomitantly, Cr diffusion is enhanced due to Cr_7C_3 coarsening, which further exacerbates the microstructural degradation. Ultimately, this evolution leads to a phenomenon wherein coarse carbides and residual austenite coexist, significantly degrading the mechanical properties of the material.

Figure 6 shows the metallographic microstructure of 42CrMo steel quenched at 860 °C after different quenching holding times. When the quenching holding time is 15 min (**Figure 6a**), austenitization is not fully carried out. There are a small amount of undissolved carbides and local ferrite residues in the microstructure, and the martensitic lath size is small and unevenly distributed, indicating that the phase transition power is insufficient.

When the holding time is increased to 30 min (**Figure 6b**), austenitization is fully completed. The degree of carbide dissolution is increased, and the martensite laths show uniformly refined characteristics, with clear grain boundaries and enhanced microstructural densification.

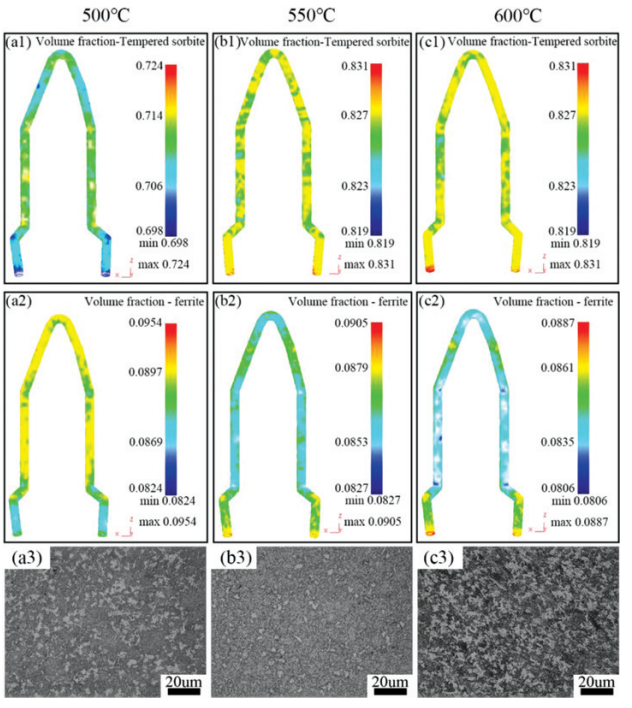

Figure 7: Microstructure cloud diagrams and metallographic structures at different tempering temperatures

After a further increase to 45 min (**Figure 6c**), austenite grains are further coarsened, resulting in a significant increase in the width of the quenched martensite laths and a slight tendency toward overheating at the grain boundaries, accompanied by traces of residual austenite in localized areas.

Figure 6d shows the Rockwell hardness of the quenched sample. It can be seen that the highest hardness of 54.1 is reached after quenching at 860 °C and holding time of 15 min. The Rockwell hardness decreases with the extension of the quenching holding time. However, excessively high hardness leads to an increase in the brittleness of the sample.

The experimental results show that 860 °C is the optimal quenching temperature for 42CrMo steel, which does not only inhibit grain coarsening but also promotes microstructural homogenization, thereby balancing the strength and toughness of the material. The 30-minute holding time is also sufficient to fully austenize the saddle hollow tube while avoiding excessive austenitization.

3.2 Tempering simulations and experiments

After setting the boundary conditions and process parameters for tempering 42CrMo steel, it was simulated that after quenching at 860 °C and oil cooling, the material was tempered at (500, 550 and 600) °C for 2 h. Microstructure distribution cloud diagrams and metallographic histograms are shown in **Figure 7**.

As the tempering temperature increased from 500 °C to 550 °C, the volume fraction of tempered sorbite significantly increased from 69.8–72.4 % to 81.9–83.1 %. This indicates that during the medium-temperature tempering stage, the precipitation of carbides and the decomposition of martensite accelerate, promoting the full formation of tempered sorbite. When the temperature further rose to 600 °C, the volume fraction of tempered sorbite tended to stabilize, and the phase transformation driving force approached equilibrium. Meanwhile, the volume fraction of ferrite exhibited a decreasing trend with an increase in the temperature, gradually decreasing from 8.24–9.54 % at 500 °C to 8.06–8.87 % at 600 °C.

Figures 7a3–7c3 show the metallographic microstructure of 42CrMo steel after being held at different tempering temperatures for 2 h. When tempered at 500 °C, a microstructure dominated by tempered troostite is formed, and finely dispersed carbides are distributed in the matrix with a high density of dislocations, providing high hardness and strength of the material, while the toughness is limited. When the tempering temperature reaches 550 °C, carbide coarsening and uniform precipitation occur. Lath martensite decomposes into tempered sorbite, and the microstructural uniformity is significantly improved, leading to the optimal balance of strength and toughness.

When the tempering temperature is 600 °C, carbides further coarsen and aggregate along the grain bound-

aries, while the matrix is dominated by ferrite. The hardness decreases dramatically, plasticity and impact toughness reach their peaks, but the strength is significantly reduced.

Figures 8a–8c show the evolution of the volume fractions of martensite, tempered martensite and tempered sorbite with tempering time during the tempering of 42CrMo steel. P1–P4 from **Figure 8** show the microstructures of the four characteristic nodes of 42CrMo steel after tempering at 550 °C for 2.5 h. It can be observed that after the start of tempering, the volume fraction of residual martensite decreases rapidly with the extension of the tempering time. In addition, the pinning effect of carbon atoms is enhanced by the formation of fine needles through the short-range diffusion of ε-carbides, corresponding with the peak volume fraction of tempered martensite (e.g., as high as 70 % in **Figure 8b**).

The beginning of the tempering and holding stage is at 3500 s. It starts after the sample has completely cooled down and the simulated tempering temperature reaches 550 °C.

With further extension of the tempering time, ε-carbide is gradually dissolved, and carbide is uniformly precipitated in the ferrite matrix. The percentage of tempered sorbite is significantly increased (**Figure 8c**), and the coarsening of carbide weakens the pinning effect of dislocations. The rate of hardness decline slows down. Near the end of the tempering stage, carbide spheroidization is completed, and the volume fraction of tempered sorbite tends to stabilize. Its final average percentage reaches 82.5 %, forming a typical tempered sorbite-ferrite dual-phase structure,[25] which is in line with the medium-carbon steel-tempering softening mechanism. This structure which does not have any obvious coarse carbides or tempered martensite residue, which is in line with the expected effect of tempering.

By comparing and analyzing the metallographic structures (**Figure 8** P1–P4) and XRD patterns (**Figure 9**) of 42CrMo steel after tempering at (500, 550 and 600) °C, it is found that at 500 °C, the structure is mainly composed of tempered troostite with a distinct slatted morphology, and a small amount of granular undissolved ferrite, accompanied by the dispersion and precipitation of fine Fe_3C carbides. The XRD pattern exhibits prominent, characteristic Fe3C peaks, indicating that carbide precipitation dominates the initial stage of martensite decomposition. The presence of trace Cr_7C_3 peaks suggests that chromium was initially involved in the carbide formation.

When tempered at 550 °C, the microstructure forms a more typical tempered sorbite structure. The carbide particles are slightly larger than those tempered at 500 °C, and their distribution is slightly sparser. The corresponding XRD patterns demonstrate significantly enhanced Cr_7C_3 peak intensities alongside weakened Fe_3C peaks, reflecting chromium's enhanced diffusion capacity that preferentially forms thermally stable Cr_7C_3 phases, while Fe_3C is partially dissolved.

At a high temperature (600 °C), tempering carbides are significantly coarser, the ferrite matrix completes the recrystallization, coarse tempered sorbite is formed, car-

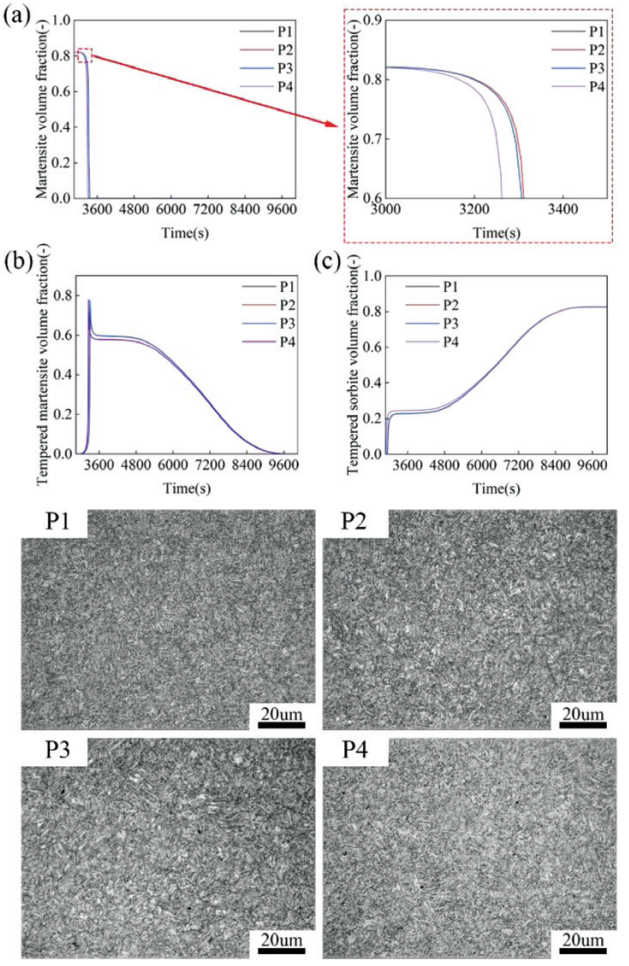

Figure 8: Variation in the microstructure and metallographic organization of characteristic nodes during tempering

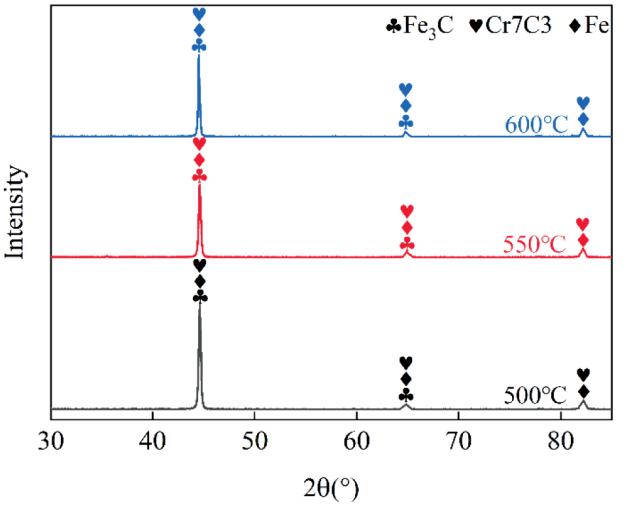

Figure 9: XRD pattern of 42CrMo steel with different tempering temperatures

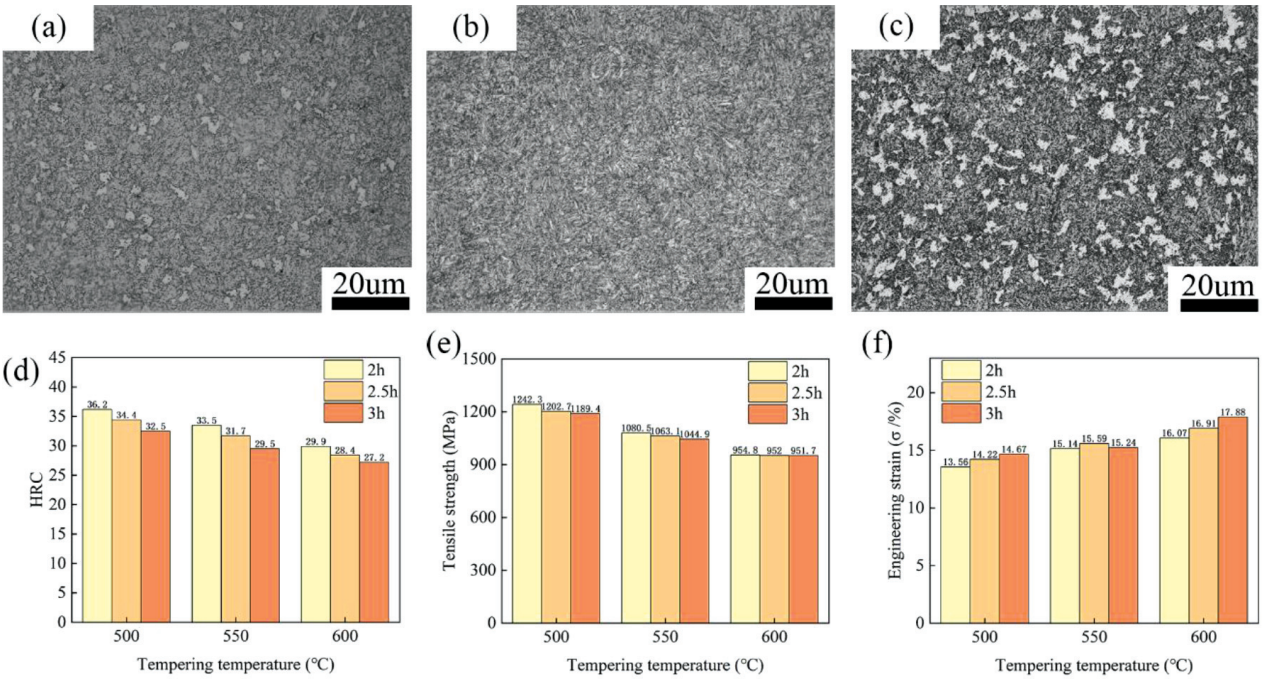

Figure 10: Metallographic structure of 42CrMo steel tempered at 550 °C for different holding times, as well as the Rockwell hardness, tensile strength and elongation of the tempered specimens

bide particle size increases, and so does the spacing. XRD spectra exhibit dominant Cr_7C_3 peaks with further diminished Fe_3C signals, confirming that high-temperature tempering promotes the Cr_7C_3 stabilization.

Figure 10 shows the metallographic structure of 42CrMo steel after tempering at 550 °C for different tempering holding times. When the tempering holding time is 2 hours (**Figure 10a**), there is carbide initial precipitation, exhibiting a fine size and disperesed distribution. The tempered sorbite matrix still retains part of the lath martensite residual structure. The grain boundary contour is fuzzier, and the microstructural uniformity has not yet been fully stabilized. The material exhibits a higher hardness but toughness is slightly insufficient. When the tempering time is 2.5 h (**Figure 10b**), carbide coarsens significantly and the distribution is uniform. Martensite laths are completely decomposed into typical tempered sorbite, ferrite matrix grain boundaries are clear, the microstructural densification is enhanced, while strength and toughness reach optimum values. When the tempering holding time is extended to 3 h (**Figure 10c**), carbide further coarsens and there is local grain boundary deviation. Matrix ferrite grains grow slightly, the microstructural uniformity is slightly reduced, the material hardness is also further reduced, while plasticity and toughness continue to improve, but the loss of strength is increased.

Figures 10d, **10e**, and **10f** show the Rockwell hardness, tensile strength, and elongation of the tempered specimens. It can be seen that with the increase in the tempering temperature and tempering holding time, the Rockwell hardness and tensile strength show a decreasing trend, and there is a significant tempering softening phenomenon, while the elongation increases accordingly. This is mainly attributed to the increase in the tempered sorbite content, which ensures better toughness and plasticity of the hollow tubes.

The experiments show that the optimal tempering temperature of 42CrMo steel saddle hollow tubes is 550 °C, and the optimal tempering holding time is 2.5 h, ensuring the best comprehensive mechanical properties.

4 CONCLUSIONS

Three-dimensional finite element modeling was carried out for a 42CrMo steel saddle hollow tube. JMatPro was used to numerically simulate the material properties of 42CrMo steel, and DEFORM was used to numerically simulate the heat treatment process. The main conclusions are as follows:

(1) After quenching at 860 °C and a holding time for 30 min, followed by oil cooling and tempering at 550 °C for 2.5 h, the comprehensive mechanical properties of the 42CrMo steel saddle-shaped hollow tube reach optimum values.

(2) When quenching is completed, the volume fraction of martensite accounts for approximately 81 % according to the simulation results. Due to the oil-cooling rate, a small portion of austenite transforms into bainite and ferrite, which is in line with the theoretical prediction of the CCT curve. After tempering is completed, most of the microstructure of the specimen transforms into tempered sorbite, with an average proportion of 82.5 %. In the actual experiment, a typical tempered sor-

bite-ferrite biphase microstructure is formed, which is in line with the expected effect of quenching and tempering, and the simulation is basically consistent with the experiment.

(3) Four characteristic nodes at different locations on the saddle hollow tube are selected, and in the numerical simulation of heat treatment, the microstructural evolution processes of P1 (outer wall node) and P2 (inner wall node) are similar, while the effect of the wall thickness on the saddle hollow tube is small. In the bend region, although stress concentration occurs at the P3 node, its evolution remains highly consistent with of the first two nodes. The P4 node in the straight tube region exhibits more prominent changes, and its microstructural phase change rate is significantly higher than for the other nodes. However, after the end of the tempering stage, the volume fraction of each microstructure is similar to those of the remaining three nodes.

Contribution

Pei Weichi: Writing - original draft, Conceptualization;
Zhang Jiawang: Experimental, Investigation, Conceptualization.
Yu Rongli: Review & editing, Conceptualization,
Liu Shengqiang: Experimental, Conceptualization, Review & editing.
Xing Menglong: Review & editing, Investigation, Conceptualization.
Ji Hongchao: Experimental, Conceptualization, Review & editing, Project administration.

Funding

This work was supported by the Scientific Research Project of Colleges and Universities in Hebei Province (CXY2024054), and funded by the S&P Program of Hebei (Grant No. 22281802Z).

Data availability

It declares that no data or materials are available for this research.

Code availability

It declares that codes are not available for this research.

Declarations

Ethics approval: The authors claim that there are no ethical issues involved in this research.

Consent to participate: All the authors consent to participate in this research and contribute to the research.

Consent for publication: All the authors consent to publish the research.

There are no potential copyright/plagiarism issues involved in this research.

Conflict of interest

The authors declare no competing interests.

5 REFERENCES

[1] H. Ji, H. Duan, Y. Li, W. Li, X. Huang, W. Pei, Y. Lu, Optimization of the working parameters of as-forged 42CrMo steel by constitutive equation-dynamic recrystallization equation and processing maps, Journal of Materials Research and Technology, 9 (**2020**) 4, 7210–7224, doi:10.1016/j.jmrt.2020.04.078

[2] G. Sui., Z. Wang, X. Fang, G. Gao, C. Zhao, Y. Guo, Y. Song, F. Jiang, Ratchetting-fatigue behavior of a 42CrMo steel under near-yield mean stress, International Journal of Mechanical Sciences, 247 (**2023**), 108166, doi:10.1016/j.ijmecsci.2023.108166

[3] G. Sui, Z. Wang, J. Li, C. Zhao, F. Jiang, H. Li, Roles of microstructures in high-cycle fatigue behaviors of 42CrMo high-strength steel under near-yield mean stress, International Journal of Fatigue, 177 (**2023**), 107928, doi:10.1016/j.ijfatigue.2023.107928

[4] J. Zhang, Z. Liu, J. Sun, H. Zhao, Q. Shi, D. Ma, Microstructure and mechanical property of electropulsing tempered ultrafine grained 42CrMo steel, Materials Science and Engineering: A., 782 (**2020**),139213, doi:10.1016/j.msea.2020.139213

[5] Y. Li, Z. Jiang, L. Li, P. Wang, D. Li, W. Xue, D. Duan, Wear behavior and damage characterization for AISI 52100 bearing steels: Effect of hardness and spherical carbides, Journal of Materials Research and Technology, 30 (**2024**), 8359–8370, doi:10.1016/j.jmrt.2024.05.220

[6] W. Huang, H. Zhong, L. Lei, G. Fang, Microstructure and mechanical properties of multi-pass forged and annealed 42CrMo steel, Materials Science and Engineering: A., 831 (**2022**), 139213, doi:10.1016/j.msea.2021.142191

[7] S. Liu, C. Cui, D. Zhang, C. Wang, X. Wang, Strength degradation of 42CrMo steel in a thermal field and its characterization method, Materials Letters, 274 (**2020**), 128031, doi:10.1016/j.matlet.2020.128031

[8] M. M. Bilal, K. Yaqoob, M. H. Zahid, Ehsan ul haq, W. H. Tanveer, A. Wadood, Effect of austempering conditions on the microstructure and mechanical properties of AISI 4340 and AISI 4140 steels, Journal of Materials Research and Technology, 8 (**2019**) 6, 5194–5200, doi:10.1016/j.jmrt.2019.08.042

[9] H. Ji, J. Wang, Z. Wang, Y. Li, Effect of martensitic variant selection on the crystallographic features of bainite/martensite multiphase structure of 42CrMo steel, Journal of Materials Research and Technology, 30 (**2024**), 9561–9571, doi:10.1016/j.jmrt.2024.06.049

[10] L. Lv, L. Fu, S. Ahmad, A. Shan, Effect of heavy warm rolling on microstructures and mechanical properties of AISI 4140 steel, Materials Science and Engineering: A., 704 (**2017**), 469–479, doi:10.1016/j.msea.2017.07.089

[11] F. Qin, H. Qi, Study on Microstructure and Properties of 42CrMo Bearing Ring in Cast-rolling Forming and Subsequent Quenching and Tempering, Journal of Mechanical Engineering, 53 (**2017**) 2, 26–33, doi:10.3901/jme.2017.02.026

[12] M. H. Khani Sanij, S. S. Ghasemi Banadkouki, A. R. Mashreghi, M. Moshrefifar, The effect of single and double quenching and tempering heat treatments on the microstructure and mechanical properties of AISI 4140 steel, Materials & Design, 42 (**2012**), 339–346, doi:10.1016/j.matdes.2012.06.017

[13] Y. Qin, X. Wang, J. Zhou, Crack formation mechanism of 42CrMo automobile steering knuckle heat treatment, Journal of Plasticity Engineering, 31 (**2024**) 8, 216–224, doi:10. 3969 / j. issn. 1007-2012. 2024. 08. 026

[14] Y. Wang, Z. Tang, Y. Yang, Development of 42CrMo tempered steel for wind power yaw guide plates, Rolled Steel, 37 (**2020**) 1, 24–29, doi:10.13228/j.boyuan.issn1003-9996.20190012

[15] Y. Wang, Y. Luo, Q. Mo, B. Huang, S. Wang, X. Mao, L. Zhou, Failure analysis and improvement of a 42CrMo crankshaft for a

heavy-duty truck, Engineering Failure Analysis, 153 (**2023**), 107567, doi:10.1016/j.engfailanal.2023.107567

[16] A. D. da Silva, T. A. Pedrosa, J. L. Gonzalez-Mendez, X. Jiang, P. R. Cetlin, T. Altan, Distortion in quenching an AISI 4140 C-ring – Predictions and experiments, Materials & Design, 42 (**2012**), 55–61, doi:10.1016/j.matdes.2012.05.031

[17] D. Qian, B. Ma, G. Dang, Numerical simulation and experimental study on grain evolution in the whole process of forging-rolling-forming-waste heat quenching of 42CrMo rings, Journal of Plasticity Engineering, 29 (**2022**) 11, 1–7, doi:10. 3969 / j. issn. 1007-2012. 2022. 11. 001

[18] Y. Gao, W. Chen, L. Wang, Organizational transformation of 42CrMo steel heavy commercial vehicle front axle during quenching process, Journal of Plasticity Engineering, 23 (**2016**) 5, 179–184, doi:10 3969/i issn 1007-2012 2016 05. 030

[19] D. Bhuyan, G. V. S. Sastry, S. Patra, S. K. Pradhan, R. Manna, Effect of austempering time on bainite plate thickness and variant selection in a high carbon low alloy steel, Materials Characterization, 200 (**2023**), 112923, doi:10.1016/j.matchar.2023.112923

[20] W. F. Hosford, ed., Iron and Steel., Cambridge University Press, New York 2012, 137

[21] M. Cakir, A. Oezsoy, Investigation of the correlation between thermal properties and hardenability of Jominy bars quenched with air–water mixture for AISI 1050 steel, Materials & Design, 32 (**2011**) 5, 3099–3105, doi:10.1016/j.matdes.2010.12.035

[22] C. Lv, L. Xu, C. Shi, Effect of Al on the hardenability and organization of 42CrMo bolt steel, Journal of Metals, 56 (**2020**) 10, 1324–1334, doi:10.11900/0412.1961.2020.00045

[23] X. C. Li, J. X. Zhao, J. H. Cong, R. D. K. Misra, X. M. Wang, X. L. Wang, C. J. Shang, Machine learning guided automatic recognition of crystal boundaries in bainitic/martensitic alloy and relationship between boundary types and ductile-to-brittle transition behavior, Journal of Materials Science & Technology, 84 (**2021**), 49–58, doi:10.1016/j.jmst.2020.12.024

[24] T. Zhou, H. Yu, S. Wang, Effect of microstructural types on toughness and microstructural optimization of ultra-heavy steel plate: EBSD analysis and microscopic fracture mechanism, Materials Science and Engineering: A, 658 (**2016**), 150–158, doi:10.1016/j.msea.2016.02.001

[25] J. Chen, W. Mo, P. Wang, S. Lu, Effects of tempering temperature on the impact toughness of steel 42CrMo, Acta Metallurgica Sinica – Chinese Edition, 48 (**2012**) 10, 1186–1193, doi:10.1016/j.engfracmech.2023.109051